Coupled Modal Simulation of a Composite Propeller Blade Subjected to Steady and Dynamic Loading

Ramona Barber, Antoine Ducoin, Stuart Wildy, John Codrington, Alban Leroyer

Sixth International Symposium on Marine Propulsors
smp'19, Rome, Italy, May 2019

Coupled Modal Simulation of a Composite Propeller Blade Subjected to Steady and Dynamic Loading

Ramona B Barber[1], Antoine Ducoin[1], Stuart J Wildy[2], John D Codrington[2], Alban Leroyer[1]

[1]Laboratoire d'Hydrodynamique, Energétique et Environnement Atmosphérique (LHEEA), École Centrale de Nantes, France
[2]College of Science and Engineering, Flinders University, Australia

ABSTRACT

The use of fiber-reinforced polymer composites in marine propellers has recently been extensively investigated, as these materials provide excellent strength- and stiffness-to-weight ratios, improved fatigue performance, and reductions in corrosion, noise generation, and magnetic signature. Another advantage of composites is their increased mechanical flexibility relative to metals and thus their capacity to deform based on flow conditions, rotational velocity, and laminate design. Despite their advantages, however, advanced composite propellers are complex and their behavior is difficult to characterize. In order to fully optimize the performance and control of these blades, a detailed understanding of the dynamic coupling between the hydroelastic response of a composite blade and the surrounding flow under a wide variety of operating conditions is required.

This work will present a numerical, fully-coupled fluid-structure interaction (FSI) study of a single composite propeller blade. The simulations are carried out using the Fine/Marine computational fluid dynamics solver to predict the flow behavior, which is coupled with a modal approach to capture structural deformations. Both static and dynamic coupling are tested, and the full hydrodynamic response is anayzed; experiments in a towing tank will follow. This paper aims to fully characterize the experimental setup and measurement system and to present the expected findings. Then, the combined experimental and numerical method will be used to validate an efficient FSI coupling method able to capture dynamic response of the composite blade submitted to unsteady flow conditions.

Keywords

Fluid-structure interaction, Modal analysis, Marine composites, Marine propellers

1 INTRODUCTION

Marine propellers have traditionally been manufactured from metallic alloys; however, the use of fiber-reinforced polymer (FRP) composites in marine propellers has recently been extensively investigated. These composite materials provide excellent strength-to-weight and stiffness-to-weight ratios, improved fatigue performance, and reductions in corrosion, noise generation, and magnetic signature (Pemberton et al 2018). Another advantage of composites is their increased mechanical flexibility relative to metals and thus their capacity to deform based on flow conditions, rotational velocity, and laminate design. This ability to deform permits passive or active shape control, where elastic changes in blade shape are tailored to improve performance over a wide range of operating conditions. Passive shape adaptation, in which material anisotropy is exploited to induce elastic twisting deformations that vary dynamically with loading, has been widely applied in marine rotor applications (Young et al 2016). Additonally, variable-stiffness materials such as shape memory alloys or piezoelectric stiffeners can be used instead of or in conjunction with passive blade adaptation to create an active shape control method to improve performance over a greater range of operating conditions (Kapuria & Das 2018, Chen et al 2017).

Despite their advantages, advanced FRP composite propellers are complex and their behavior is difficult to characterize. In order to fully optimize the performance and control of these blades, a detailed understanding of the dynamic coupling between the hydroelastic response of a composite blade and the surrounding flow under a wide variety of operating conditions is required. In addition, advanced composite blades are vulnerable to flaws such as voids or delaminations, as well as damage caused by impact, vibration, twisting, and fatigue. Unfortunately, the initiation and evolution of the complex failure modes in advanced composite structures are difficult to accurately characterize; furthermore, damage to FRP composites is often impossible to determine by visual inspection.

Real-time monitoring of performance and blade shape can both provide feedback for advanced control systems and be used to detect and characterize damage. For that purpose, embedded fiber Bragg grating (FBG) sensors have shown great potential for *in-situ* mechanical measurements. Fiber optics are lightweight, small in size, effectively immune to electromagnetic interference, and have been proven to successfully measure strain in composite hydrofoils (Wildy et al 2010, Phillips et al 2017, Cook et al 2017). FBG arrays have also been used to detect and characterize damage in FRP composites (Yeager et al 2016, 2017) and have been studied for structural health monitoring systems in marine applications (Seaver et al 2006). Integrated with a calibrated numerical model, FBG sensors may provide further improvements to damage prediction and on-line performance analysis in composite hydrofoils (Cook et al 2017,

Ward et al 2018). However, most studies on FBG sensor arrays in FRP composites have focused on simplified beam sections or hydrofoils. Few studies have taken into account the complexities associated with the highly twisted geometry of a marine propeller.

In order to successfully apply a real-time monitoring strategy, however, the performance and deformation of the blade in question must be fully understood under a wide range of operating conditions. This work will present a numerical, fully-coupled fluid-structure interaction (FSI) study of a propeller blade and experimental setup that will be later used to develop an on-line monitoring method for composite propellers. This knowledge will be essential in subsequent steps to create a method to extrapolate full-field blade deformation in real time from limited optical fiber data, which can in turn be used to inform control strategies and to detect damage or delaminations. At this point, the objective of the work is to fully characterize the hydroelastic response of a single propeller blade in steady and unsteady flows using a joint numerical and experimental method.

The numerical model employed for this project combines a computational fluid dynamics (CFD) solver with a modal structural analysis directly implemented in the CFD code for a dynamic, fully coupled fluid-structure interaction analysis. This approach will be used to fully characterize the simplified system of a single, non-adaptive, non-rotating propeller blade as a requisite preliminary step before commencing experimental towing tank tests at Central Nantes, France. It is essential to highlight that, as a first step, this simplified configuration will not fully represent a rotating blade; i.e, it will not take into account the spanwise variation of velocity due to rotation. Due to the highly twisted nature of a propeller blade as compared to a hydrofoil, however, a higher level of multi-scale dynamic excitation in the flow and in the hydroelastic response of the blade can be expected. The method will later be extended to include the study of flexible, variable-stiffness, and rotating propeller blades.

2 METHODS

2.1 Experimental Configuration

The blade profile chosen for this study is the INSEAN E779A geometry (INSEAN 2006), a research profile with low skew and a fixed pitch ratio along the radius (P/D_P = 1.1). The normalized profile data was scaled to generate a single blade of length 500 mm and an overall propeller diameter of D_P = 1200 mm; however, only the blade is considered in this investigation. The blade was manufactured using a 2x2 twill weave, 199 gsm prepreg carbon fiber fabric (Cytec Industrial Materials, VTM264/CF0302-42%), with material properties as shown in Table 1. The fabric was aligned with the 0° and 90° fiber directions parallel to the blade spanwise and chordwise orientations, respectively, to create a quasi-isotropic material. Five layers of prepreg were used to give an overall laminate wall thickness of nominally 1.2mm in the main blade body, while two additional layers of fabric were added to reinforce the high stress region around the mounting system at the blade root. An optical fiber with an array of Bragg gratings was embedded for strain measurement and damage detection in each of the pressure and suction walls of the blade. The optical fiber and grating sensors run parallel to the spanwise direction and are located towards the leading edge.

Table 1: Material properies of Cytec Industrial Materials VTM264/CF0302-42%.

Elastic Modulus	Shear Modulus	Poisson's Ratio
E_1 = 60 GPa	G_{12} = 3.9 GPa	ν_{12} = 0.04
E_2 = 60 GPa	G_{23} = 2.7 GPa	ν_{23} = 0.3
E_3 = 6.9 GPa	G_{13} = 2.7 GPa	ν_{13} = 0.3
Orthotropic Stress Limits		
X_T = 700 MPa	X_C = -540 MPa	XY = 95 MPa
Y_T = 700 MPa	Y_C = -540 MPa	YZ = 65 MPa
Z_T = 50 MPa	Z_C = -170 MPa	XZ = 65 MPa

The experimental part of this study will take place in the towing tank at Centrale Nantes. The towing tank is 140 m long by 5 m wide with a constant depth of 3 m; the tank carriage has a maximum velocity of 8 m/s. The blade is fixed to a rigid frame surrounded by a foil section with longitudinal rails designed to reduce the impact of the free surface on the blade. The blade orientation can be altered during the tests; in this case, hydroelastic blade response and dynamic coupling at angles of 0° (as defined by zero lift generation) to 12° are explored. At the root of the blade, a hydrodynamic balance is installed to measure forces and moments as well as an accelerometer to capture vibrations. A schematic of the test setup is shown in Figure 1.

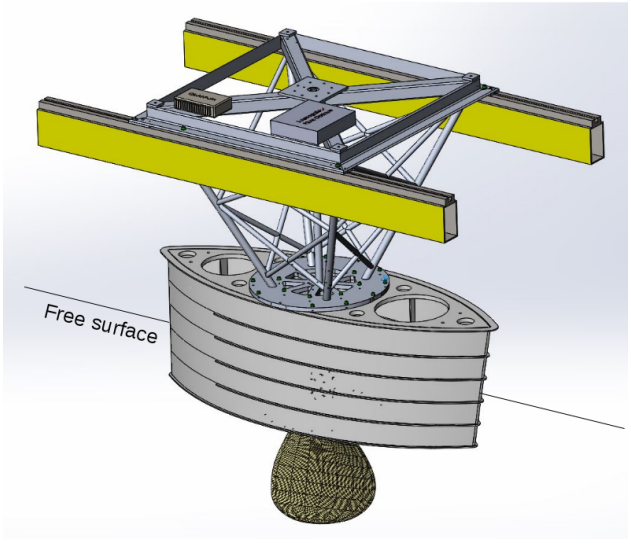

Figure 1: Experimental test setup.

2.2 Numerical Methods

The numerical modeling performed for this study use a fully-coupled FSI approach with a structural modal analysis coupled to a CFD solver. The FSI simulation combines the computational fluid dynamics solver Fine/Marine (ISIS-CFD 2018), developed at Centrale Nantes, France, with a modal structural analysis solved initially in the commercial finite element software ABAQUS (ABAQUS 2014) and directly implemented in the CFD code.

2.2.1 Computational Fluid Dynamics Solver

The CFD code ISIS-CFD in Fine/Marine (ISIS-CFD 2018) solves the incompressible Unsteady Reynolds-Averaged Navier-Stokes (URANS) equations in a strongly conservative manner. It uses a fully-unstructured, cell-centered finite-volume method to build the spatial discretization of the conservative equations. Further details of the solver can be found in Mouton et al (2018) and Leroyer et al (2008).

Two CFD domains were considered in this study. The first domain considers the full test setup as shown in Figure 1, and fully represents the free surface with a volume of fluid method. The reduced domain considers only the blade, with a horizontal plane with a symmetry condition (i.e, $\vec{V} \cdot \vec{n} = 0$) set parallel to the root section. The two domain boundaries are defined with rectangular boxes that extend $6c_{max}$ upstream and $9c_{max}$ downstream of the blade location and $5c_{max}$ beyond the blade tip and to each side. A refinement box is placed $\pm$ $1c_{max}$ in the cross-stream and upstream directions and $3c_{max}$ downstream to fully resolve the wake. A far field velocity boundary condition was applied upstream, to the sides and below the blade, while the downstream outlet was set at proscribed pressure. A $k-\omega$ SST turbulence transport model was employed. Grid and time step independence were verified before running the complete computations. The final mesh contains 6.2 million elements in the full domain and 2.2 million for the simplified domain; the mesh on the blade surface is shown in Figure 2. Time steps for dynamic analyses of approximately dt = 0.001 s were used, adjusted according to the freestream velocity to maintain a similar Courant number across calculations. In this study, blade angles of α = 0° to 12° are studied at inflow velocities of V = 1 to 4 m/s, for a range of Reynold's numbers between $Re = 3.3 \cdot 10^5$ and $13.3 \cdot 10^5$.

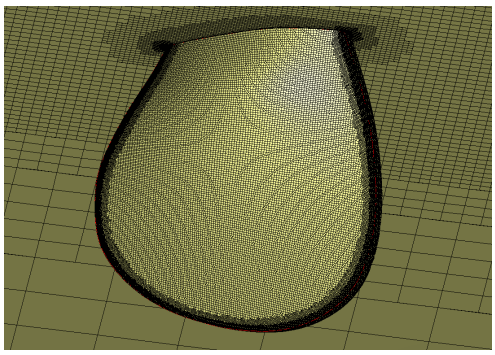

Figure 2: CFD mesh on the INSEAN E779A propeller blade.

2.2.2 Fluid-Structure Interaction with Modal Approach

To carry out the FSI coupling, a modal approach is used. Modal analysis allows the simplification of the linearized governing equation of motion of size n using the eigen modal matrix. Assuming Rayleigh damping, the eigen modal matrix allows the diagonalization of the mass and damping matrices; normalizing the eigen mass matrix simplifies the problem into a resolution of n uncoupled single-DOF systems in the form

$$\ddot{q}_i + 2\epsilon_i \omega_i \dot{q}_i + \omega_i^2 q_i = \phi_i^T f(t) \tag{1}$$

where ϕ_i is the i^{th} modal vector, q_i is the associated amplitude, $\omega_i = 2\pi f_i$, the natural frequency, ϵ_i is the damping coefficient and $f(t)$ the loads acting on the system. The total deformation of the system is then given by

$$\sum_{i=1}^{n} q_i(t)\phi_i(x) \tag{2}$$

These equations are fully coupled with the resolution of the fluid flow, as added mass effects (defined as the part of the pressure force proportional and opposed to body acceleration) are naturally included in the calculation of the fluid force. However, with the low ratio of structural to fluid densities in this example, added mass effects can introduce significant numerical instabilities in the model. While a CFD solver cannot itself separate the true added mass effect from the total fluid force, an artificial added mass method is added via an internal implicit coupling algorithm, in order to better capture the energy exchange at the interface and to ensure stability of the algorithm. For each eigenmode i, an added mass coefficient is estimated and added to both sides of the equation, such that the final equation to solve for the non-linear sub-iteration k is as follows

$$\begin{aligned}(1 + a_i)\ddot{q}_i|_{t+dt}^{k+1} + 2\epsilon_i \omega_i \dot{q}_i|_{t+dt}^{k+1} + \omega_i^2 q_i|_{t+dt}^{k+1} \\ = \phi_i^T f(t)|_{t+dt}^{k} + a_i \ddot{q}_i|_{t+dt}^{k}\end{aligned} \tag{3}$$

The addition of the added mass coefficient thus decreases the dependency of the right hand side on the body acceleration, acting as a relaxation step. At convergence, $a_i^{k+1} = a_i^k$ and the original equation is recovered. It is therefore not necessary to accurately estimate the coefficient a_i; however, as the modal added mass estimate approaches the actual modal mass, convergence properties improve. For this reason, the solver evaluates the modal mass directly for each degree of freedom at the beginning of the computation and can update it dynamically if desired.

The deformation of the structure is thus solved and the mesh updated within one time step. ISIS-CFD takes as input the shapes and frequencies of the first m natural modes of vibration of the structure in air, allowing the reduction of the model by excluding modes that do not have a significant impact on the case studied. The coupled model is solved in time with options for both a quasi-steady and

fully unsteady approach, allowing the user to optimize the solver for computational efficiency or high resolution.

2.2.3 Modal Analysis

In this simulation, the commercial finite element software ABAQUS (ABAQUS 2014) is used to solve for the modal shapes and frequencies. The deformed shape as determined by the sum of the amplitudes of the given mode shapes in the CFD solver is then returned to ABAQUS during post-processing via a user-defined subroutine in order to analyze the structural response of the blade. The finite element representation of the blade has approximately 6k 4-node reduced integration shell elements (S4R).

To validate the calculated modal shapes and frequencies, a 1D Scanning Laser Doppler Vibrometer was used to capture the natural frequencies and vibration shapes of the experimental blade. The numerically calculated mode shapes of the first four modes are compared to the experimental values in Figure 3, and the corresponding frequencies are shown in Table 2. High correlation was found in the mode shapes and the frequencies were within acceptable bounds. The difference between the numerical and experimental frequencies for the fourth mode are not insignificant; this is likely due to numerical stiffening relating to the complex mode shape. The importance of each progressive mode shape, however, is strongly reduced from the previous; for that reason the discrepancy in the fourth modal frequency is considered negligible.

Table 2: Modal frequency values.

Experimental	Numerical	Difference
56 Hz	60 Hz	7%
99 Hz	97 Hz	2%
154 Hz	164 Hz	6%
186 Hz	210 Hz	13%

In order to determine the appropriate number of structural modes to employ in the FSI model, a single study was performed repeatedly with an increasing number of modes. The change in deformation between each case was calculated. Figure 4 shows the evolution of the analysis at several locations along the blade radius. Though a significant majority of the displacement is captured with the first two modes, mode shapes 3 and 4 clearly influence the twist of the blade. Higher modes add little to the overall displacement or twist except at the very tip of the blade, which is small enough to be extremely sensitive to very small changes. This does not affect the overall performance; change in lift between a 4-mode study and higher was measured at less than 1%. Thus, the final coupled analysis employs the first four natural vibration modes of the structure.

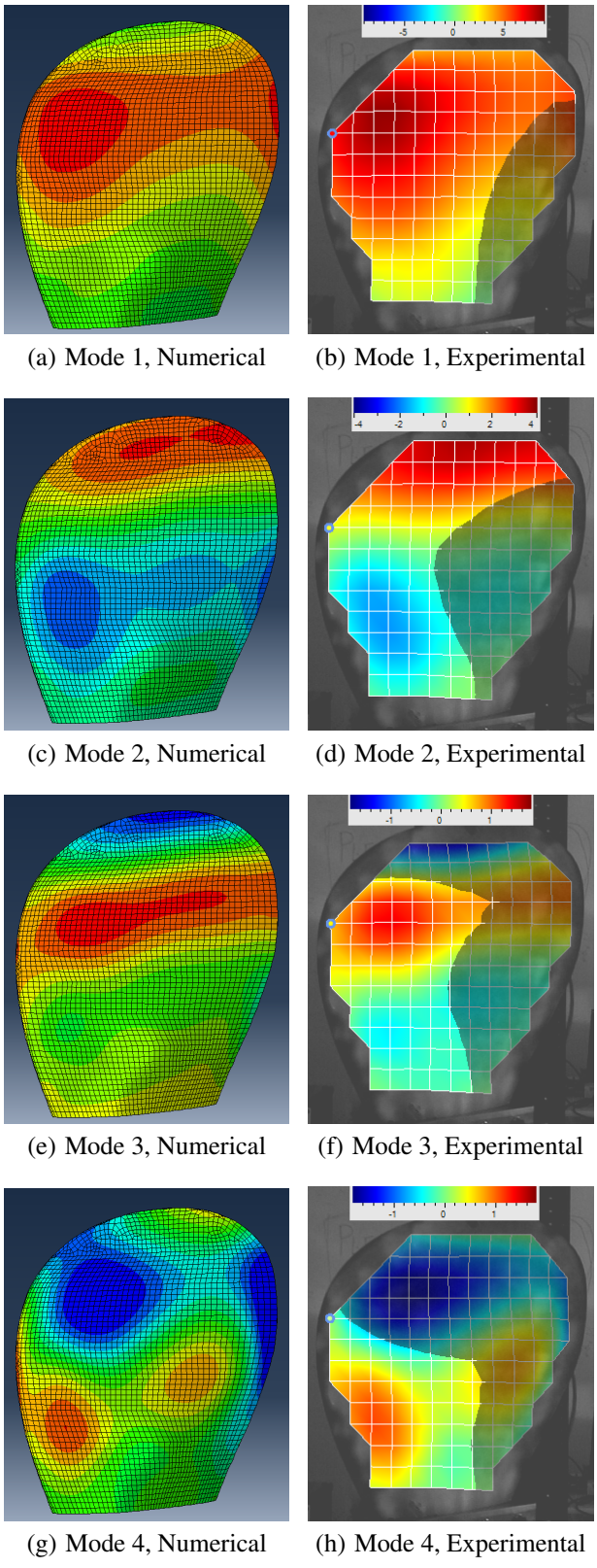

(a) Mode 1, Numerical (b) Mode 1, Experimental

(c) Mode 2, Numerical (d) Mode 2, Experimental

(e) Mode 3, Numerical (f) Mode 3, Experimental

(g) Mode 4, Numerical (h) Mode 4, Experimental

Figure 3: Numerical and experimental mode shapes shown from the suction side and shaded by relative displacement magnitude. The gray region on experimental figures is an artifact of the laser alignment and is not significant to the results.

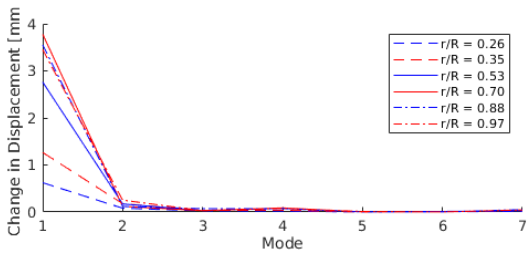

(a) Change in displacement on leading edge nodes

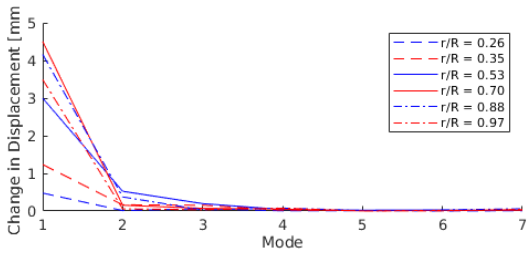

(b) Change in displacement on trailing edge nodes

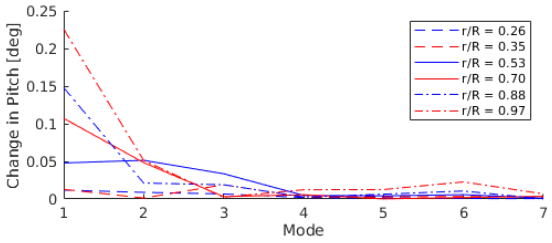

(c) Change in pitch

Figure 4: Change in displacement and pitch with each mode added to the calculation at several spanwise sections along the lenth of the blade.

3 RESULTS

3.1 Rigid Blade CFD Results

Before implementing the coupled FSI analysis, it is necessary to evaluate the results of the CFD solver alone. This is effectively an analysis that assumes the blade and support system are fully rigid. Once rigid-blade performance is determined, a coupled analysis can be added for comparison.

It was initially assumed that the foil surrounding the blade support structure adequately reduced the influence of the free surface on the blade performance to a point that the free surface could be neglected in models. In order to verify that assumption, the full system including the foil and the free surface was modeled and compared to a single-fluid analysis of the blade alone. Slight differences in the pressure field were noted, as shown in Figure 5, particularly on the suction side near the root where the flow detachment interacts with the plate boundary layer in the full model. A difference of 3.2% in the lift force was calculated between models ($C_L = 0.346$ including the foil and 0.335 without); this difference was considered acceptable given the reduction in computational expense of nearly 90% between the full and reduced models.

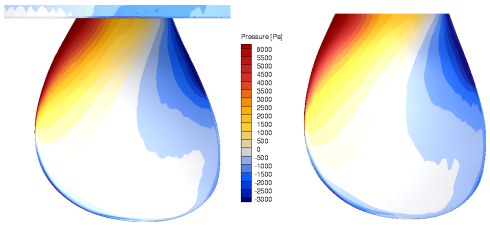

(a) Pressure side

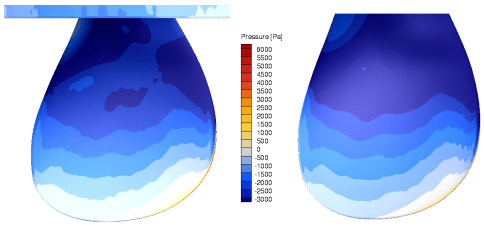

(b) Suction side

Figure 5: Comparison of pressures calculated on the full (right) vs. simplified (left) domains for the blade at $\alpha = 12^\circ$ and V = 4 m/s.

The full system analysis also showed that the foil with longitudinal rails successfully reduced the impact of the superstructure on the incident flow directly upstream of the blade. The free surface elevation, shown in Figure 6, remains at all points above the level of the test section, and the coefficient of friction along the bottom of the foil, shown in Figure 7, confirms that the flow is fully attached leading up to the blade (positive friction coefficient). While the flow does detach from the bottom of the foil near the leading edge of the blade, that can be related to the detachment caused by the high angle of attack at the blade root. Therefore, impact of the free surface and support structure on the blade performance was determined to be negligible and these features were not modeled in later simulations.

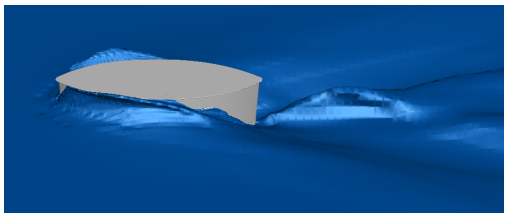

(a) Free surface elevation, top view

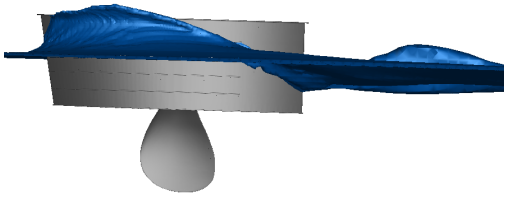

(b) Free surface elevation, side view

Figure 6: Influence of foil on free surface elevation and velocity.

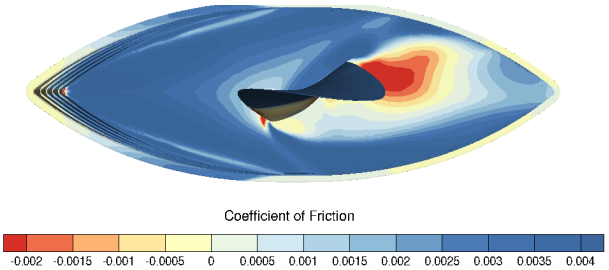

Figure 7: Coefficient of friction on the bottom of the support foil.

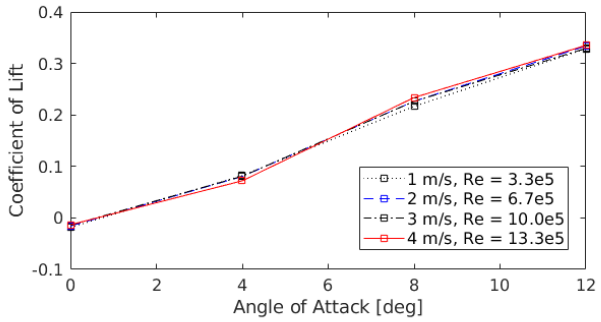

(a) Coefficient of Lift

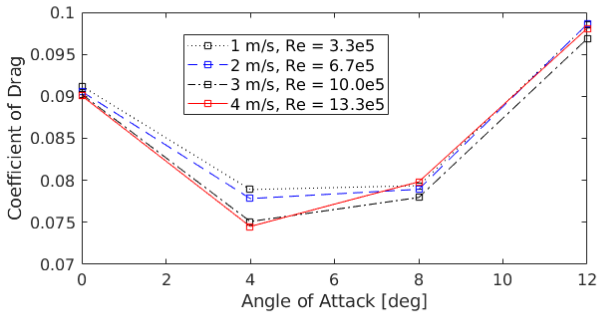

(b) Coefficient of Drag

Figure 8: Blade performance as a function of angle of attack at various inflow velocities.

After the simplified domain was established, calculations were performed to establish a baseline rigid-blade performance for the system; the results of these calculations are shown in Figure 8. The influence of inflow velocity (equivalent to Reynold's number sensitivity in a rigid blade analysis) on the coefficient of lift is slight. A slightly larger variation is seen in the drag coefficient, as well as a significant drop in drag between α = 0° and α = 4°. This is due to the fact that at 0°, the flow along the blade is mostly detached and the blade is acting more like an obstruction in the flow than a foil. Otherwise, the increase in drag with angle of attack advances as expected.

Due to the lack of blade rotation, this test setup is closer to a highly twisted hydrofoil rather than a true propeller blade, causing flow detachment at various locations along the blade depending on the operating condition. The evolution of the flow attachment with angle of attack at V = 4 m/s is shown in Figure 9. At α = 0°, the flow is slightly detached near the root at the trailing edge on the suction side, shown, and also on the pressure side of the blade, as evidenced by the streamlines crossing behind the blade in the figure. As the angle of attack increases, the detachment at the trailing edge grows significantly.

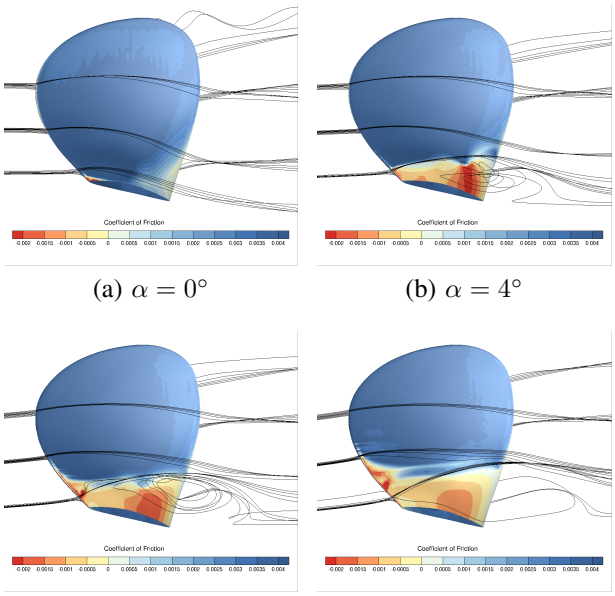

(a) $\alpha = 0°$ (b) $\alpha = 4°$

(c) $\alpha = 8°$ (d) $\alpha = 12°$

Figure 9: Coefficient of friction at V = 4 m/s with streamlines shown at r/R = 0.25, 0.5, and 0.75.

3.2 Coupled FSI Results

The results of the quasi-static FSI analyses are compared to the rigid-blade results in Table 3. At α = 8° and 12°, the change in performance when the deformation of the blade is considered is slightly negative and increases in magnitude with increasing velocity as expected, as the blade flexes to comply with the flow. However, there is a large positive change in the coefficient of lift between the rigid and coupled cases for the analyses at $\alpha = 4°$. This initially seems surprising; it is therefore necessary to examine the case in a fully dynamic analysis.

Figure 10 shows the results of the dynamic calculation for $\alpha = 4°, V = 4m/s$. In Figure 10(a), the coefficients of lift and drag along with the maximum displacement are shown over a period of 0.5 s. The data exhibit a strongly periodic behavior due to partial vortex shedding observed in Figure 9(b). In comparison to Table 3 above, the average C_L is 0.076 : a 6.6% decrease from the value found in the rigid calculations, which is more more in line with the trends from the other cases. It is clear from the large fluctuations in the forces that this is a highly unsteady case and thus a quasi-steady calculation cannot accurately capture the dynamic coupling behavior.

In Figure 10(b), the variation of each modal contribution

Table 3: Results of coupled calculations.

Operating Condition	C_L Coupled	C_L Rigid	% Difference	Max. Displacement	Max. Δ Pitch
4°, 3 m/s	0.113	0.081	+28.4 %	1.60 mm	-0.09°
4°, 4 m/s	0.097	0.072	+25.7 %	2.87 mm	-0.16°
8°, 3 m/s	0.218	0.226	-3.8 %	1.79 mm	-0.08°
8°, 4 m/s	0.220	0.234	-6.5 %	3.19 mm	-0.15°
12°, 3 m/s	0.320	0.329	-2.9 %	2.62 mm	-0.11°
12°, 4 m/s	0.319	0.335	-5.1 %	4.64 mm	-0.19°

is shown over the same time span; the mean modal contributions are shown in Table 4. The main forcing frequency due to the dynamic loading is apparent, as well as the higher frequency vibrations in the higher modes. Please note the difference in scale between the variations in the first mode and the higher modes; the range of variation in the first mode is an order of magnitude higher than the others. Though the mean value for the second mode amplitude is higher, the contribution from the first mode ends up defining a large majority of the deformation due to the hydrodynamic excitation evidenced by the fluctuation in the lift coefficient. Moreover, the added mass effect reduces the first natural frequency to a value near the vortex shedding frequency, suggesting a possible interaction between the flow and the first mode.

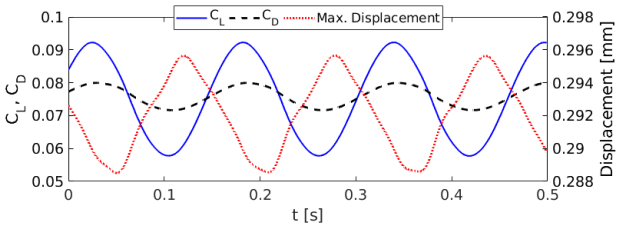

(a) Coefficients of lift and drag, maximum displacement

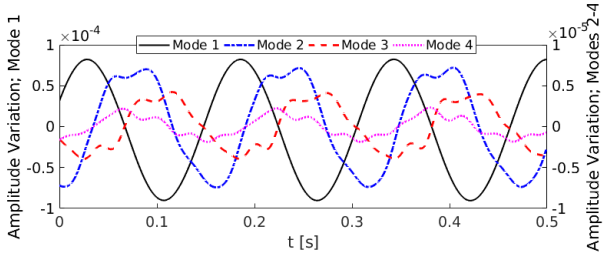

(b) Modal amplitude variation

Figure 10: Results of dynamic analysis for $\alpha = 4°$, $V = 4m/s$.

Table 4: Mean modal amplitudes.

Mode	1	2	3	4
Mean Amp.	8.4e-5	-1.1e-3	-2.9e-5	-4.4e-5

Overall, the magnitude of the calculated deformation indicates that it will be possible to capture the changes in shape with the optical fiber system. The FSI analysis does not indicate a significant difference in blade pitch; this likely means the change in performance is due to a deformation of blade camber. It is important to note that changes in performance could be in part due to numerical features rather than fully physical; this possibility will be examined in further dynamic analyses and the experimental studies.

Finally, it is possible to examine the strains at the level of the optical fibers, between the fourth and fifth (outermost) plies of the composite layup, as shown in Figure 11. Although the deformation at the blade root is not large, there is a significant strain concentration at the leading edge of the root and, to a lesser extent, along the trailing edge at this level in the material. This shows the importance of a full structural analysis before the implementation of the optical fiber sensors; it is necessary to place the fibers such that it is possible to capture the strain concentrations without subjecting the fibers to excess loading.

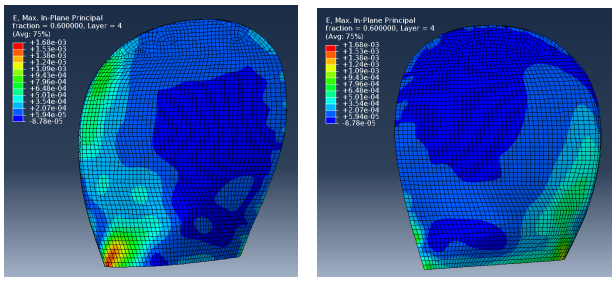

(a) Suction side (b) Pressure side

Figure 11: Instantaneous strain at the ply level of the optical fibers at 12° and 4 m/s.

4 CONCLUSIONS AND FUTURE WORK

Despite their advantages, advanced composite propellers are complex and their behavior is difficult to characterize. In order to fully optimize the performance and control of these blades, a detailed understanding of the dynamic coupling between the hydroelastic response of a composite blade and the surrounding flow under a wide variety of operating conditions is required. In this work, a fully-coupled fluid-structure interaction study of a non-rotating propeller blade is presented. This numerical study is used to fully characterize the performance and deformation of an experimental setup that will be later used to develop an on-line

monitoring method for composite propellers.

First, the structural model was validated by comparing modal shapes and frequencies to experimental results. Good agreement was found between both the frequency values and the mode shapes. A numerical study was performed in order to select the number of modes necessary to capture blade deformations; it was shown that the use of the first four modes was adequate.

Blade performance in both rigid and coupled FSI analyses were then presented and compared, and deformations from the FSI study were examined. A strong difference in deformed blade shape was found at low angles of attack in quasi-static coupled simulations; in a dynamic analysis, this was explained as the highly unsteady flow could not be adequately captured by a quasi-static analysis.

In the future, experimental studies will be executed to validate and expand on the FSI calculations presented in this work. Optical fibers with an array of fiber Bragg gratings will be used for strain measurement and damage detection, and forces, moments, and vibrations will be captured at the blade root. These data will be used to asses the ability of the optical fiber to evaluate the static and dynamic response of the blade submitted to hydrodynamic flow.

5 ACKNOWLEDGMENTS

This research is co-funded by Flinders University, Australia and Centrale Nantes, France, under an academic collaboration agreement. The authors would like to thank the technical staff of both universities for helping with the blade and support system design.

REFERENCES

ABAQUS Version 6.14 Documentation. (2014). ABAQUS, Inc.

Chen, F., Lui, L., Lan, X., Li, Q., Leng, J. & Liu, Y. (2017). 'The Study on the Morphing Composite Propeller for Marine Vehicle. Part I: Design and Numerical Analysis'. Composite Structures **168**, pp. 746-757.

Cook, P.R., Alavija, A. & Wildy, S.J. (2017). 'Identification and characterisation of delamination damage in composites utilising embedded optical strain gauges'. Proceedings of the Ninth Australasian Congress on Applied Mechanics, Engineers Australia.

Cook, P.R., Alavija, A., Wildy, S.J. & Arkwright, J.W. (2017). 'Strain Measurement in Unidirectional Carbon Fibre Utilising Embedded Optical Strain Gauges'. Proceedings of the Ninth Australasian Congress on Applied Mechanics, Engineers Australia.

The INSEAN E779A Propeller Dataset. (2006). INSEAN Propulsion and Cavitation Laboratory.

ISIS-CFD v8.1 Theory Guide. (2018). Laboratoire de recherche en Hydrodynamique, Energétique et Environment Atmosphérique, École Centrale de Nantes.

Kapuria, S. and Das, H.N. (2018). 'Improving Hydrodynamic Efficiency of Composite Marine Propellers in Off-Design Conditions Using Shape Memory Alloy Composite Actuators'. Ocean Engineering **168**, pp. 185-203.

Leroyer, A., Barré, S., Kobus, J.-M. & Visonneau, M. (2008). 'Experimental and Numerical Investigations of the Flow Around an Oar Blade'. Journal of Marine Science and Technology **13**, pp. 1-15.

Mouton, L., Leroyer, A., Deng, G.B., Querty, P., Soler, T. & Ward, B. (2018). 'Towards Unsteady Approach for Future Flutter Calculations'. Journal of Sailing Technology **7**, pp. 2018-07.

Pemberton, R., Summerscales, J., & Graham-Jones, J. (eds.) (2018). Marine Composites: Design and Performance. Woodhead Publishing.

Phillips, A.W., Cairns, R., Davis, C., Norman, P., Brandner, P.A., Pearce, B.W. & Young, Y.L. (2017). 'Effect of Material Design Parameters on the Forced Vibration Response of Composite Hydrofoils in Air and in Water'. Proceedings of the Fifth International Symposium on Marine Propulsors, Espoo, Finland.

Seaver, M., Trickey, S.T. & Nichols, J.M. (2006). 'Strain Measurements from FBGs Embedded in Rotating Composite Propeller Blades'. Optical Fiber Sensors, Optical Society of America.

Ward, J.C., Harwood, C.M. & Young, J.L. (2018). 'Inverse Method for Hydrodynamic Load Reconstruction on a Flexible Surface-Piercing Hydrofoil in Multi-Phase Flow'. Journal of Fluids and Structures **77**, pp. 58-79.

Wildy, S., Cazzolato, B. & Kotousov, A. (2010). 'Detection of Delamination Damage in a Composite Laminate Beam Utilising the Principle of Strain Compatibility'. Key Engineering Materials **417-418**, pp. 269-272.

Yeager, M., Todd, M., Gregory, W. & Key, C. (2016). 'Assessment of Embedded Fiber Bragg Gratings for Structural Health Monitoring of Composites'. Structural Health Monitoring **16**(3), pp. 262-275.

Yeager, M., Whittaker, A., Todd, M., Kim, H., Key, C. & Gregory, W. (2017). 'Impact Detection and Characterization in Composite Laminates with Embedded Fiber Bragg Gratings'. Procedia Engineering **188**, pp. 156-162.

Young, Y.L., Motley, M.R., Barber, R.B., Chae, E.J. & Garg, N. (2016). 'Adaptive Composite Marine Propulsors and Turbines: Progress and Challenges'. Smart Materials and Structures **11**, pp. 925-939.